Princeton Plasma Physics Laboratory

**PPPL-** 5105

PPPL-5105

# ULF Waves at Mercury

Eun-Hwa Kim, Scott A. Boardsen,
Jay R. Johnson, and James A. Slavin

January 2015

**Prepared for the U.S. Department of Energy under Contract DE-AC02-09CH11466.**

# Princeton Plasma Physics Laboratory
# Report Disclaimers

---

## Full Legal Disclaimer



## Trademark Disclaimer



---

# PPPL Report Availability

## Princeton Plasma Physics Laboratory:

http://www.pppl.gov/techreports.cfm

## Office of Scientific and Technical Information (OSTI):

http://www.osti.gov/scitech/

---

**Related Links:**

**U.S. Department of Energy**

**Office of Scientific and Technical Information**

# ULF waves at Mercury

2 Eun-Hwa Kim[1,2], Scott A. Boardsen[3,4], Jay R. Johnson[1,2], and James A. Slavin[5]

4 Corresponding author: E.-H. Kim, Princeton Center for Heliophysics, Princeton University, P.O. Box 0451, Princeton, NJ 08543-0451, USA (ehkim@pppl.gov)

6

[1] Princeton Center for Heliophysics, Princeton University, Princeton, NJ 08543, USA

[2] Princeton Plasma Physics Laboratory, Princeton University, Princeton, NJ 08543, USA

[3] Goddard Planetary Heliophysics Institute, University of Maryland, Baltimore, MD 21228, USA

[4] Heliophysics Science Division, NASA Goddard Space Flight Center, Greenbelt, MD 20771, USA.

[5] Department of Atmospheric, Oceanic and Space Sciences, University of Michigan, Ann Arbor, MI 48109-2143, USA

## Abstract

Ultra-low frequency (ULF) waves are regularly observed at Mercury. A recent statistical study showed that the magnetic compressional component is dominant near the magnetic equator and the magnetic transverse component is dominant in the higher magnetic latitude. In this paper, we address possible interpretations of those waves. Because the observed waves typically exhibit linear polarization, they have been considered to be the field-line resonance (FLR) structure. When compressional waves propagate into the inner magnetosphere, they can mode convert to field-aligned waves associated with the ion-ion hybrid resonance. These transverse mode-converted waves oscillate globally reaching high magnetic latitude. Alternatively, the electromagnetic ion Bernstein wave (IBW) has been considered as another possibility because of the strong power of the compressional component. Ray-tracing calculations of the IBW modes propagating in a dipole magnetic field suggest that electromagnetic IBWs are highly unstable to the proton loss cone distribution function with field-aligned group velocity. As the waves propagate they become highly compressional even in a moderate proton $\beta$ plasma. Therefore, the compressional waves near the magnetic equator could be explained by the IBWs while transverse waves could be explained by the FLR concept.

## 1. Introduction

NASA's Mariner 10 and MESSENGER (MErcury Surface, Space ENvironment, GEochemistry, and Ranging) spacecraft missions provide a wealth of observations within Mercury's magnetosphere [e.g., *Ness et al.*, 1974, *Slavin et al.*, 2008, 2009, *Anderson et al.*, 2008, 2011], and both spacecraft detected ultra-low frequency (ULF) waves in the ion cyclotron frequency range [*Russell*, 1989; *Boardsen et al.*, 2009a, b, 2012].

The first observation of the ULF waves was detected by the Mariner 10 spacecraft during its first flyby. The narrow band waves had frequency $f \sim 0.5$ Hz [*Russell*, 1989] around 40% of the proton cyclotron frequency $f_{cP} = \Omega_P/(2\pi) \sim 1.31$ Hz. Because heavy ions from solar wind ($H^+$, $He^+$, and $He^{++}$) and planet ($Na^+$, $Mg^+$, and $Si^+$) are abundant in Mercury's magnetosphere [e.g., *Zurbuchen et al.*, 2008, 2011; *Raines et al.*, 2013, 2014], the observed wave frequency is clearly located in between heavy ion and proton cyclotron frequencies. Because the signal detected by Mariner 10 was mainly transverse to the ambient magnetic field ($\mathbf{B}_0$) with an almost linear polarization in the meridian plane, it was suggested that the pulsations were a standing Alfvén wave along the magnetic field [e.g., *Russell*, 1989; *Othmer et al.*, 1999; *Glassmeier et al.*, 2003, 2004; *Kim* and *Lee*, 2003; *Klimushkin et al.*, 2006]. However, unlike transverse Alfvén waves, the pulsation also had a strong magnetic compressional component, so it was argued that the observed waves could not be pure standing Alfvén waves [*Blomberg*, 1997; *Southwood*, 1997; *Kim et al.*, 2008].

Over 30 years later, highly coherent ULF waves with frequencies near 1 Hz were observed in Mercury's magnetosphere during the first and second flybys of the MESSENGER spacecraft [*Boardsen et al.*, 2009a, b]. The wave frequency varied between the local $He^+$ cyclotron frequency ($f_{cHe}$) and the local proton cyclotron frequency. An outbound boundary layer was

encountered on both flybys, and wave power was a factor of 10 greater inside the boundary layer than outside. Near the closest approach of each flyby trajectory, the power in the wave component oriented parallel to the local magnetic field ($B_{\parallel}$) tended to be larger than the power in the component perpendicular to the field ($B_{\perp}$), whereas the perpendicular power dominated away from the closest approach.

More recently, a statistical study of the ULF waves detected in the orbital phase of the MESSENGER spacecraft was made at frequencies in between 0.4 and 5 Hz [*Boardsen et al.*, 2012]. The survey covered 2.1 Mercury years (March 24 – September 25, 2011). The observed waves can be classified into (a) transverse component dominant (25% of the wave events) and (b) compressional component dominant (75% of the wave events).

Figure 1 shows an example of the transverse component dominant waves. During this event the transverse component ($B_{\perp}$) was dominant throughout with the wave frequency is almost constant near the 1-2 Hz. Near the magnetic equator, transverse component becomes very strong. Thus the waves are close to the local $f_{cP}$ near the magnetic equator and near or below $f_{cHe+}$ at the higher magnetic latitudes. 75% of the wave observations show that the compressional component ($B_{\parallel}$) waves are dominant. Figure 2 shows that the magnetic compression has two peaks near the magnetic equator around 17:10 UT and 17:12 UT, respectively, that straddle the model magnetic equator.

Figure 3 represents another example of ULF waves that show the mixture of transverse dominant in the higher latitude and compressional dominant near the equator. In this figure, waves transverse to the local magnetic field were first seen at intermediate magnetic latitudes (starting at 35°N), and as the spacecraft approached the magnetic equator the wave amplitude increased and the magnetic compressional component becomes stronger as the frequency

become closer to the local $f_{cP}$. Due to the weakness of Mercury's dipole moment relative to that of Earth's, the magnetic equator location (~1.3 $R_M$, where $R_M$~2440 km is Mercury's radius) can deviate significantly in latitude from the model, so it is plausible that the compressional peaks in Figure 3 straddle the true magnetic equator.

In the statistical study [*Boardsen et al.*, 2012], the ULF waves are seen at all magnetic local times (MLT), but their observed rate of occurrence is much less on the dayside than the night side as shown in Figure 4. However, this distribution of wave events could be the lack of coverage near the dayside magnetic equator. The distribution of events peaks near the magnetic equator and at a radial distance of 1.35 ± 0.13 $R_M$ and drops toward zero as the radial distance increases toward $2R_M$ (Figure 4)

The polarization characteristics have also been investigated. One of the most dominant features of the wave distribution is that the waves are strongly compressional near the magnetic equator and transverse far from the equator as shown in an example of wave event in Figure 3. This pattern can be seen in the ratio of parallel component power to total power ( $|B_\parallel|^2/|B|^2$ ) for nightside event as shown in Figure 5a. Near the magnetic equator, most values of this power ratio exceed 0.7 ($|B_\parallel|^2/|B|^2 > 0.7$), while in the higher magnetic latitude greater than 30°, this power ratio is less than 0.1 ($|B_\parallel|^2/|B|^2 < 0.1$). Figure 5b plots the ellipticity versus magnetic latitude for wave events that are strongly transverse. In order to examine ellipticity of the transverse waves, the ratio of power in the perpendicular component to total power > 0.7 (thus $|B_\parallel|^2/|B|^2 < 0.3$) has been selected. Near the magnetic equator the absolute value of the ellipticity is approximately 0.5, whereas at higher magnetic latitudes the absolute value of the ellipticity decreases toward 0 as the waves become more strongly linear.

In order to examine the ULF waves at Mercury, field-line resonance and the electromagnetic ion Bernstein waves (IBWs) have been suggested. Field-line resonances at Mercury are expected to occur at the ion-ion hybrid (IIH) resonances in the multi-ion plasmas and should have purely transverse polarization [*Kim et al.*, 2008]. When incoming fast compressional waves (FWs) match the IIH resonance condition, strong absorption of incoming FWs can occur leading to excitation of the IIH resonance [e.g., *Karney et al.*, 1979]. Numerical simulations showed that this mode-converted IIH waves are guided by the ambient magnetic field line ($\mathbf{B}_0$) and have linear polarization [*Kim et al.*, 2008, 2013, 2015].

On the other hand, *Boardsen et al.* [2012] proposed that the observed waves could be mainly composed of short wavelength (~100 km) electromagnetic IBW mode in a high proton $\beta$ plasma. Using ray tracing calculations, they confirmed that electromagnetic IBWs generated by loss cone instability can explain MESSENGER observations where the compression straddles the equator [*Boardsen et al.*, 2014a]. Although the IBWs in the ray tracing calculations can exhibit transverse polarization off the equator, they reflect at magnetic latitudes around 12°, which is much less than typically observed.

In the next sections, we will review both theories and compare the theoretical results with the observations. The field-line resonance conditions and IBW properties are introduced in Section 2 and 3, respectively, and then the last section contains the discussion and summary.

## 2. Field-Line Resonance at Mercury's Multi-Ion Magnetosphere

When $\omega << \omega_{ce}, \omega_{pe}$, where $\omega_{ce}$ and $\omega_{pe}$ are the electron gyro- and plasma frequencies, the basic description of the plasma wave is given by the approximate cold plasma dispersion relation

$$n_\perp^2 \cong \frac{(\varepsilon_R - n_\parallel^2)(\varepsilon_L - n_\parallel^2)}{(\varepsilon_S - n_\parallel^2)}, \quad (1)$$

where $n_{\|}$ and $n_{\perp}$ are refractive indices parallel and perpendicular to $\mathbf{B}_0$ respectively. $\varepsilon_R$, $\varepsilon_L$, and

116 $\varepsilon_S$ are the tensor elements for two ions [*Johnson et al.*, 1995],

$$\varepsilon_R(\varepsilon_L) \cong \frac{c^2}{V_A^2}\frac{\omega_{c1}\omega_{c2}}{\omega_{cut}}\frac{\omega \pm \omega_{cut}}{(\omega \pm \omega_{c1})(\omega \pm \omega_{c2})}, \quad (2)$$

118 $$\varepsilon_S \cong \frac{c^2}{V_A^2}\frac{\omega_{c1}^2\omega_{c2}^2}{\omega_{bb}^2}\frac{\omega^2 - \omega_{bb}^2}{(\omega^2 - \omega_{c1}^2)(\omega^2 - \omega_{c2}^2)}, \quad (3)$$

where $\omega = 2\pi f$ is an angular frequency, $V_A$ and $\omega_{cut}$ are the Alfvén velocity and the cutoff

120 frequency for $\varepsilon_R = 0$ or $\varepsilon_L = 0$, respectively. This approximate dispersion relation has a resonance when $n_{\perp} \to \infty$ and two cutoffs when $n_{\perp} \to 0$. The resonance condition is determined

122 from Eq. (1),

$$n_{\|}^2 = \varepsilon_S, \quad (4)$$

124 and the cutoff conditions are

$$n_{\|}^2 = \varepsilon_{R(L)}. \quad (5)$$

126 The resonance in Eq. (4) is called as the Alfvén resonance, perpendicular ion cyclotron resonance, or ion-ion hybrid resonance depending on wave frequency. In the MHD

128 approximation, the wave frequency is much lower than the heaviest ion cyclotron frequency, and Eq. (4) is reduced to the Alfvén resonance,

130 $$\omega_A = k_{\|} V_A, \quad (6)$$

where $k_{\|}$ is a wavenumber parallel to $\mathbf{B}_0$. The resonant absorption of MHD waves in an

132 inhomogeneous magnetosphere has been well investigated [e.g., *Tamao*, 1965; *Uberoi*, 1972; *Chen* and *Hasegawa*, 1974]. When incident FWs propagate across an Alfvén velocity gradient, it

134 can couple with the shear Alfvén wave, at the location where the phase speed parallel to $\mathbf{B}_0$ is

equal to the local Alfvén speed seen in Eq. (6) and the wave energy is transferred from the FW to a shear Alfvén wave propagating along the magnetic field [*Hasegawa et al.*, 1983]. At Earth's magnetosphere, because the magnetic field lines are bounded by the ionosphere, shear Alfvén waves have an eigenmode structure along magnetic field lines such that only a discrete spectrum of frequencies are associated with a field line. Assuming the Alfvén velocity varies smoothly, the frequency of each discrete mode varies continuously across the field lines and this discrete spectrum of waves is called a field line resonance (FLR) [*Chen and Hasegawa*, 1974, *Southwood*, 1974].

By adopting the FLR concept, *Russell* [1989] initially proposed that the detected pulsation from Mariner 10 was a standing Alfvén wave along a background $\mathbf{B}_0$, because the signals were primarily transverse to $\mathbf{B}_0$. Using an electron density of 3 $cm^{-3}$ and assuming an electron-proton plasma with the measured field strength, he derived an Alfvén velocity of about 1000 km/s. With a field line length of 4000 km based on a dipole model, *Russell* [1989] also estimated that the fundamental frequency of a standing wave on the field line would be about 0.125 Hz. Accordingly, the observed 0.5 Hz wave could be the fourth harmonic of the fundamental wave.

However, because the observed wave frequency (38% of $f_{cP}$) by Mariner 10 is well outside the MHD frequency range, the MHD approximation is not applicable for these observations. At higher frequency ($f \sim f_{cP}$), plasma waves should be described using a multi-fluid approach.

For $f \sim f_{cP}$ in an electron-proton plasma, the Alfvén resonance is generalized to the perpendicular ion cyclotron resonance (or Alfvén resonance) from Eq. (4),

$$\omega_A^2 \cong \frac{k_\parallel^2 V_A^2}{(1 - k_\parallel^2 V_A^2 / \omega_{cH}^2)}, \tag{7}$$

which is the frequency modified Alfvén resonance [e.g., *Stix*, 1992]. At the frequency modified Alfvén resonance, wave energy transfers from the FW to the shear Alfvén wave and the ion

158 cyclotron wave analogous to the MHD case [e.g., *Karney et al.*, 1979; *Winglee*, 1982; *Kim* and *Lee*, 2003]. By adopting a two fluid wave model, *Kim* and *Lee* [2003] examined the behavior of
160 the Alfvén resonance when $f \sim f_{cP}$ and discussed the implications for waves at Mercury in a single ion plasma.

162 When multiple ion species are included in the plasma, there are two additional resonances between each part of cyclotron frequencies: (a) the Buchsbaum resonance for perpendicular
164 propagation [*Buchsbaum*, 1960], where

$$\varepsilon_S(f_{bb}) = 0, \tag{8}$$

166 where $f^2_{bb} = f_{c1} f_{c2} (f_{c1} \eta_2 + f_{c2} \eta_1) / (f_{c1} \eta_1 + f_{c2} \eta_2)$ is the Buchsbaum resonance frequency and $\eta_{ion} = N_{ion}/ N_e$ where $N_{ion(e)}$ is an ion (electron) number density and (b) the ion-ion hybrid (IIH)
168 resonances for oblique propagation, [e.g., *Lee et al.*, 2008; *Kim et al.*, 2008] where Eq (4) is satisfied,

170 $$n_{\parallel}^2(f_{ii}) = \varepsilon_S(f_{ii}), \tag{9}$$

where $f_{ii}$ is the ion-ion hybrid resonance frequency. At these resonances, the absorption from the
172 FWs to a field-aligned resonant mode occurs, and both resonances provide important features that have been associated with ULF waves at Earth [e.g., *Johnson et al.*, 1995, *Horne* and *Thorne*,
174 1997, *Johnson* and *Cheng*, 1999, *Lee et al.*, 2008, *Kim et al.*, 2009].

In multi-ion plasmas at Mercury, a necessary condition for resonant mode coupling has been
176 derived and it is the same as the IIH resonance [*Othmer et al.*, 1999; *Glassmeier et al.*, 2003, 2004; *Klimushkin et al.*, 2006]. They had also suggested that the crossover frequency
178 ( $f_{cr}^2 = \eta_1 f_{c2}^2 + \eta_2 f_{c1}^2$ ), is the preferred frequency for the FLR at Mercury when this frequency is satisfied at the resonance condition, thus $f = f_{ii} = f_{cr}$.

Using a model appropriate for the magnetic field and plasma composition at Mercury, *Kim et al.* [2008] demonstrated that FLRs at Mercury should occur when the ion-ion hybrid (IIH) and/or Alfvén resonance conditions are satisfied. Assuming that the plasma inhomogeneity and $\mathbf{B}_0$ lie in $x$ and $z$ direction in the slab coordinate system, respectively, Figure 6 shows time histories of the perturbed electric (**E**) and magnetic (**B**) fields at the IIH resonance point in the electron-proton-sodium plasma [*Kim et al.*, 2008]. In this figure, the $E_x$ and $B_y$ component grow in time, while the other wave components ($E_y$, $B_x$, and $B_z$) damp. These results clearly show that the FWs are mode converted into IIH waves near the IIH region where $f \sim f_{ii}$, and the magnetic field of FLRs at Mercury's magnetosphere oscillates linearly in the east-west meridian, which is similar to FLR at Earth [e.g., *Lee and Lysak*, 1989]. Later, these results were extended to the electron-proton-$He^{++}$-$Na^{+}$ plasma [*Kim et al.*, 2013].

However, in these simulations the inhomogeneity responsible for the mode conversion was a 1D inhomogeneity in the heavy ion concentration with a homogeneous magnetic field. More realistically, the mode conversion may also result from the gradient in the magnetic field strength, and 2D effects in dipolar geometry may play an important role especially given the global extent of the wave observations. For inhomogeneous $B_0$ in dipolar geometry, fast wave energy remains most concentrated at the magnetic equator and mode conversion occurs at surfaces of constant magnetic field strength for fixed ion concentrations. Mode conversion primarily occurs at the magnetic equator where the fast mode wave energy concentrates. As the mode converted wave propagates along field lines to regions to higher latitude where the magnetic field strength increases, it encounters the cutoff where $n_{\parallel}^2(f_{bb}) \cong \varepsilon_S(f_{bb}) \to 0$, and ion cyclotron resonance where $n_{\parallel}^2(f_{ci}) \cong \varepsilon_S(f_{cj}) \to \infty$ [*Johnson et al.*, 1989, 1995]. Thus the propagation characteristics of the IIH waves along $\mathbf{B}_0$ will be different from that of homogeneous $B_0$ plasmas, where the

cutoff and resonance would not be encountered. A two-dimensional finite element wave code in multi-fluid plasmas, which solves the full wave equations in global magnetospheric geometry, has recently been developed [*Kim et al.*, 2015] to explore the effects of inhomogeneity in the magnetic field. Using this code, *Kim et al.* [2015] investigated how field-aligned propagating ULF waves at Mercury can be generated by externally driven FWs via mode conversion at the IIH resonance and how such waves globally oscillate.

Figure 7 shows the wave solutions from the 2D wave model [*Kim et al.*, 2015]. In this figure, both the FW and the mode-converted IIH wave modes are clearly seen. The FW mode appearing in all electromagnetic components is directly launched near ($r_{ext}$, $z_{ext}$) = (2 $R_M$, 0) and propagates away from the source toward the inner and outer magnetosphere. Because the FW mode is launched near the magnetic equator (point A in Figure 7b), the waves propagating toward the inner magnetosphere partially reflect near $r/R_M$ = 1.43, where the cutoff condition of the FW mode is satisfied (point B in Figure 7b). The remainder of the energy penetrates deep into the magnetosphere and totally reflects at Mercury's surface due to the reflecting boundary condition. The FWs reflected from Mercury's surface propagate to the outer magnetosphere with different propagation angle (point C in Figure 7b) and are eventually absorbed near the outer boundary. A numerical collisional layer has been added near the outer boundary to ensure that outgoing waves do not reflect back into the domain.

On the other hand, the IIH resonant waves appear only in $E_\eta$, $E_b$, and $B_\varphi$ in Figure 7, where the unit vector $\hat{b}$ is along the magnetic field line, $\hat{\varphi}$ is the azimuthal direction, and $\hat{\eta}$ is normal to the field line pointing outward. In this figure, IIH waves show long wavelength in the field-aligned direction and fine structure in the perpendicular direction for $1.4<L_M<1.8$, where $L_M$ is

Mercury's L-shell. Because the waves launched at $L_M$=2 are pure FW modes, the waves showing field-aligned structures in $E_\eta$ and $B_\varphi$ are unmistakable evidence of mode conversion.

In Figure 7, *Kim et al.* [2015] also over-plots the locations where $f = f_{bb}$, which corresponds to the cutoff of the field-aligned propagating IIH waves. Waves at larger radial distance encounter the cutoff location before they reach higher latitude, but because the mode converted wave is able to penetrate the evanescent region between Buchsbaum resonance to the ground, wave power can reach the surface where it reflects and sets up a global oscillation similar to the field-line resonance at Earth [e.g., *Lee* and *Lysak*, 1989], although it is weakly damped Conversely, field-line resonance occurs at Mercury when the IIH resonance conditions are satisfied [e.g., *Kim et al.*, 2008], and because such resonances globally oscillates, they reach higher magnetic latitudes.

In order to determine how efficiently wave absorption occurs at Mercury, *Kim et al.* [2011] evaluated the absorption coefficients at the IIH resonance for variable concentrations of sodium ($\eta_{Na}$) and azimuthal ($m_y$) and field aligned wave harmonic numbers ($m_z$) using 1D full wave model. They found that the absorption at the IIH resonance occurs for a broad range of parameters of $\eta_{Na}$, $m_y$, and $m_z$, and is also very sensitive to wave number and the ion concentration ratio. Thus they suggested that the radial profile of field-line resonances at Mercury can exhibit complex, discontinuous structure.

In order to examine wave absorption in the various L-shell, using a 1D full wave model [*Kim et al.*, 2011], we also calculate the absorption coefficient as a function of (a) $L_M$ and $\eta_{Na}$ for $f$ = 0.95 Hz and (b) $\Omega = f / f_{cP}$ and $\eta_{Na}$ at $L_M$ = 1.75 for $m_y$ = 0 as shown in Figure 8. The figure clearly shows that strong absorption occurs in a wide range of $\eta_{Na}$, $L_M$, and $\Omega$, which is consistent with *Kim et al.* [2011]. The results can be summarized as: strong absorption occurs (a)

where $1.4 \leq L_M \leq 1.8$ for $\eta_{Na} = 15\%$ and $f = 0.95$ Hz in Figure 8a, which is consistent with the 2D full wave calculation in Figure 7 (b) where $0.1 \leq \Omega \leq 0.65$ for $L_M = 1.75$ and $\eta_{Na} = 15\%$ in Figure 8b, and (c) where $7\% < \eta_{Na} < 49\%$ for $L_M = 1.75$ and $f = 0.95$ Hz in Figure 8a-b. Because the absorption of FW modes corresponds to the generation of IIH waves, it has been suggested that IIH waves detected by spacecraft can be used to infer heavy ion density ratio [*Kim et al.*, 2008; *Kazakov* and *Fülöp*, 2013]. However, strong absorption in a wide range of $\eta_{Na}$ at a single magnetic field line in Figure 8 leads to the conclusion that the heavy ion density ratio cannot be simply inferred from the frequency of field-aligned IIH waves at Mercury.

In this section, we introduce how field-aligned propagating ULF waves at Mercury can be generated by externally driven FWs via mode conversion at the ion-ion hybrid resonance. The mode-converted IIH waves are strongly guided by $\mathbf{B}_0$ and have linear polarization. Simulations in dipole magnetic field show how IIH waves can reach higher magnetic latitudes over 40° for realistic magnetic field and densities at Mercury and how they globally oscillate. These results are consistent with the observed waves that can propagate over magnetic latitude of 40° with strong magnetic transverse component and linear polarization seen in Figure 1-2 [*Boardsen et al.*, 2012]. Simulations also show that mode conversion occurs in a wide range of L-shell for a single frequency wave, which is also consistent with wave observation. For instance, strong transverse waves near 1 Hz are found in $1.3 \leq L_M \leq 1.8$ and $0 < \text{MLT} < 42°$ by both observation (Figure 1) and simulation (Figure 7).

## 3. Ion Bernstein Waves

Although the concept of FLR can explain many of these observations, strong magnetic compressibility cannot be explained by this theory. The mixture of compressional waves and the mode converted waves may occur, but FLR cannot explain the waves that are compressionally

dominant ($|B_{\parallel}|^2/|B|^2 > 0.5$), about ~75% of all observations [*Boardsen et al.*, 2012]. These waves can have up to 4 harmonics (Nyquist frequency limited). Figure 2 and Figure 3 show examples of waves that are highly compressional near the magnetic equator. In these figures, it should be noted that the magnetic compression maximizes slightly away from equator (with maxima straddling the equator). In Figure 3 the "true equator" crossing is believe to be shifted from the model equator crossing, the minimum in $B_0$ occurs around 2:38UT.

We summarize the results of the wave propagation study of the ion-Bernstein wave (IBW) mode by *Boardsen et al.* [2014a]. *Boardsen et al.* [2012] proposed that these highly compressional waves are IBW mode waves in a high proton $\beta$ plasma (~2). For the observed values of $\beta$ *Denton et al.*[2010] noted that the IBW mode around peak growth rate develops a strong magnetic compression. However, based on an analysis of data obtained from the plasma instrument on the MESSENGER spacecraft it was shown that the proton $0.1<\beta<0.5$ in the regions where these waves are observed [*Boardsen et al.*, 2014a], with proton $\beta$ in the range 0.1 to 0.2 near 1.35 $R_M$, where the occurrence peaks in Figure 4c. In this range the IBW mode around the peak growth rate shows weak to moderate compression [*Denton et al.*, 2010; *Gary et al.*, 2010].

Because the occurrence of these compressional waves peaks around 1.35 $R_M$, large planetary loss cones are expected and have been found in the proton data [*Boardsen et al*., 2014a]. At these radial distances on the nightside typical values for the proton density are 1–3 $cm^{-3}$ with temperatures around 1 keV. Mercury has no plasmasphere, due to the lack of and ionosphere and a very weak co-rotational electric field, therefore the cold plasma contribution to the ion population is believed to be negligible. Of course if there were a cold plasma component present, then these waves could be explained by the "fast magnetosonic mode" which is strongly

compressional [*Boardsen et al.*, 2014b] and its dispersion relation is given by the extraordinary mode in cold plasma theory [*Stix*, 1992].

Figure 9a shows the proton distribution function where the loss cone distribution is approximated by the difference of two bi-Maxwellians with a $\beta$ of 0.135 used as input to the warm plasma dispersion solver WHAMP (Waves in Homogeneous Anisotropic Multi-component Magnetized Plasma) [*Rönnmark*, 1982]. The black dot with the vertical bar in Figure 9a, which lies in a region with positive perpendicular gradient, indicates where the protons in velocity space strongly interact with waves at maximum growth rate (point A in Figure 9b). The index of refraction curve that contains maximum growth rate is plotted on top of the growth/damping rate of the dispersion surface. Around the peak growth rate the solution is consistent with solutions found in the Earth's plasma sheet boundary layer [*Denton et al.*, 2010; *Gary et al.*, 2010]. The branch of the index of refraction surface labeled A-B in Figure 9b is characterized by strong growth with weak to moderate magnetic compression, consistent with the findings of *Denton et al.*[ 2010] and *Gary et al.* [2010]. The branch labeled B-D in Figure 9b is characterized by weak damping and strong magnetic compression. On branch A-B, $k_{||}V_{G||}$ is positive ($k_{||}V_{G||} >0$), while on branch B-D, $k_{||}V_{G||}$ is negative ($k_{||}V_{G||} <0$), where $V_{G||}$ is the group velocity parallel to $\mathbf{B}_0$. This fact is important in understanding the strange cyclic propagation behavior of the waves in magnetic latitude shown in Figure 10.

*Boardsen et al.* [2014a] called these waves the IBW mode because the wave vector is nearly perpendicular to the background magnetic field, the wave electric field is strongly aligned in the wave vector direction, and the peak wave growth is near a harmonics of the proton cyclotron frequency. As noted by *Denton et al.* [2010] and *Boardsen et al.* [2014a], these waves are not electrostatic because the $E/(cB)$ ratio is below one ($E/(cB) <1$), peaking around 0.25 at the

maximum compression. It is pointed out that the phase velocity of this mode is ~100 km/s compared to a proton thermal speed of ~1000 km/s so the real part of the dispersion relation cannot be approximated by cold plasma theory for these short wavelength waves of ~100 km.

Using RATRACE [*Rönnmark*, 1984], warm plasma ray tracing of this mode was performed by *Boardsen et al.* [2014a] as shown in Figure 10. In this preliminary study, they assumed an electron-proton plasma with a constant density and dipole magnetic field throughout the ray-tracing volume. The ray was launched with a wavevector and frequency consistent with the peak growth rate at the magnetic equator. The group velocity for this mode is highly field-aligned except around points B and D in Figure 9b (if the index of refraction surface were drawn to scale it would appear as horizontal line in Figure 9b and for weak dissipation the group velocity is perpendicular to the index of refraction surface).

The ray launched at the magnetic equator (with peak growth rate at point A in Figure 9b) propagates away from the equator. As the ray moves outwards in magnetic latitude in Figure 10a, its location on the index of refraction surface slides toward point B in Figure 9b. As the ray moves around point B onto the B-D segment of the index of refraction surface $V_{G||}$ changes sign (the sign of $k_{||}$ does not change) and the ray starts to propagate back toward the magnetic equator. The "cusp like" shape of the reflection point in Figure 10 is due to the "cusp like" shape of the index of refraction surface at point B in Figure 9b.

If the ray reaches point D in Figure 9b on the index of refraction surface before reaching the equator the sign of $V_{G||}$ will change as $k_{||}$ goes through zero and the wave will start to propagate away from the magnetic equator on the D-B segment. When point B in Figure 9b is reached on the index of refraction surface the sign of $V_{G||}$ changes sign again and the ray propagates back to

the magnetic equator on the B-A segment and continues into the southern hemisphere where this strange cyclic behavior repeats in the other hemisphere.

Of course the shape of index of refraction surface will change as the ray propagates. For this simple model, *Boardsen et al.* [2014a] found that the index of refraction surface retained the general features shown in Figure 9b, a segment A-B with large growth rate and moderate compression and a segment B-D with near zero damping and large compression, and a sharp cusp formed by the intersection of the curves A-B and B-D. For higher proton $\beta$ around 0.5 *Boardsen et al.* [2014a] found another cycle where compression peaks upon crossing the magnetic equator, but in general the proton $\beta$ tends to be around 0.1 to 0.2 where the majority of the compressional waves observations are observed.

*Boardsen et al.* [2014a] also found that the group velocity drops as the waves propagate through peak compression leading to a pile-up of compressional wave energy density. Looking at Figure 10a one sees compression peaking off the magnetic equator at ±7° consistent with the observations. They also found that the wavelength is much smaller than the spatial scale lengths suggesting that the WKB approximation is reasonable, but they pointed that in principle the pile up of the wave energy while propagating through peak compression could violate the WKB approximation, and studies using full wave solutions are needed around peak compression.

The observed wave frequency ratio to the proton cyclotron frequency ($\omega/\Omega_p$) for the fundamental of 3 events studied by *Boardsen et al.* [2014a] were between 0.63 and 0.76 near peak compression, while theory predicts at peak growth that this ratio is between 0.93 and 0.97 (depending on electron temperature) for the parameter range used in their study. *Boardsen et al.* [2014a] pointed out that at peak linear growth rate the perpendicular component of the group velocity $V_{G||}$ is ~40 km/s. The magnitude of $V_{G||}$ lies in the range of the $E \times B$ drift velocity based

362 on estimates of the cross-tail electric field [*DiBraccio et al.*, 2013]. If $V_{G\|}$ is directed against the drift velocity their sum could be small leading to optimal growth in Mercury's frame of
364 reference. For this orientation one predicts a Doppler shift that can explain this discrepancy. They also noted that $\omega/\Omega_p$ drops to 0.8 at peak compression which can account for about 1/2 of
366 the difference.

Here, we reviewed the interpretation that the strong magnetic compressional waves near $f_{cP}$
368 and its harmonics observed with 20° of Mercury's magnetic equator could be the IBW mode. *Boardsen et al.* [2014a] show that the proton loss-cone distributions are highly unstable to the
370 IBW mode. They found that the index of refraction surface, where the maximum growth rate appears, is composed of two line segments, one segment consists of high growth rate and low
372 magnetic compression, and the other branch consists of small damping rate and is highly compressional (Figure 9b). As the IBW mode propagates in magnetic latitude (Figure 10) they
374 switch between the branches. For the dominate mode of cyclic propagation the compression maximizes at ±7° about the magnetic equator consistent with the observation of many equatorial
376 crossings by MESSENGER (e.g., Figure 2). At peak compression the group velocity drops which would lead to a pile up of compressional wave energy.

378 *Boardsen et al.* [2014a] reconciled the difference between linear modeling $\omega/\Omega_P$ at the model peak growth rate and the observed $\omega/\Omega_P$ around peak compression as due to the Doppler shift.
380 They also point out that about 1/2 the difference can be accounted for by the change in this ratio as the wave propagates from peak growth rate to peak compression (Figure 10).

## 382 4. Discussion and Summary

In this review, we provided a brief overview of the observed characteristics of ULF waves at
384 Mercury. A recent statistical study of ULF waves at Mercury based on MESSENGER data

[*Boardsen et al.*, 2012] reported the occurrence and polarization of the detected waves. The waves are usually observed between radial distances of 1.1 to 1.8 $R_M$ with maximum occurrence near $R_M \sim 1.4$ and between magnetic latitudes of ± 40° with strong occurrence near the magnetic equator. These waves are also detected primarily on the night side with two maximum peaks around MLT 6 and 21. Measurements of wave polarization indicate that the waves are mostly compressional near the magnetic equator, but the transverse component is dominant at latitudes greater than ~ 20°. The transverse fluctuations are also linearly polarized.

We also introduced the field-line resonance and the electromagnetic ion Bernstein waves to explain such waves and we showed that both theories can partially explain the observations. When the FW mode is launched in the outer magnetosphere, the waves propagate to inner magnetosphere and strong field-aligned waves are mode-converted at the IH resonance. Such mode-converted IIH waves globally oscillate, and thus reach higher magnetic latitude with transverse and linear polarization, which is consistent with observations at higher magnetic latitude. The ray-tracing calculations explored the propagation of the IBW mode in a dipole magnetic field and found that the electromagnetic IBWs are highly unstable to the proton loss cone distribution function and the wave's group velocity is highly field aligned. As the waves propagate they can become highly compressional even in a moderate proton $\beta$ ~0.05 to 0.54 plasma. Therefore, the compressional waves near the equator and transverse waves in the higher latitudes can be explained by IBWs and FLR, respectively.

Although both theories obtained general characteristics of waves detected at Mercury, much work remains. First, *Kim et al.* [2008, 2015] used a cold plasma model even though kinetic effects in hot plasmas are believed to be important for the generation and propagation of ULF waves at Mercury [e.g., *Glassmeier et al.*, 2003; *Slavin et al.*, 2009; *Boardsen et al.*, 2012,

2014a]. In hot plasmas, the FW mode can be converted into the short wavelength IBW or ion cyclotron wave modes (or their higher harmonics) at the IIH resonance [e.g., *Wukitch et al.*, 2005]. The mode-converted IBW modes have short-wavelength in the radial direction and long-wavelength in field-aligned direction, thus the mode-converted IBW mode is expected to propagate at large normal angle because of $k_\perp >> k_\parallel$. Therefore, a short wavelength IBW mode at Mercury could be either externally generated via mode conversion at the IIH resonance or internally generated from plasma instability [*Boardsen et al.*, 2014a]. It should be noted that the wave occurrence is much higher near the magnetic equator than off the equator and wave characteristics at higher latitude are mainly transverse while near the equator the waves are strongly compressible. Thus the compressionally dominant waves near the magnetic equator could be mixed with internally generated and externally mode-converted IBW modes while waves at higher magnetic latitudes could be mode-converted IIH waves (or IBWs).

At Mercury, various heavy ion species, such as $He^+$, $He^{++}$, $Na^+$, $Mg^+$, and $Si^+$, are abundant. However, previous studies used a simple plasma density model. *Kim et al.*, [2015] assumed electron-proton-$Na^+$ plasmas with constant $Na^+$ density ratio. When lighter ions ($He^+$ and $He^{++}$) are included, the cutoff condition of the field-aligned waves (the Buchsbaum resonance) shifts toward the outer magnetosphere and lower magnetic latitude. In addition, depending on the heavy ion density ratios, the wave stop gap between the locations where $f = f_{bb}$ and $f = f_{ci}$ becomes wider or narrower. Figure 11 shows the dispersion relation ($n_\parallel^2 = \varepsilon_S$) of the IIH waves along the magnetic field line at $L_M$=1.4 for 2% and 15% $He^{++}$ or 15% $Na^+$ plasmas and the stop gap between $f_{bb}$ and $f_{cHe++}$ is clearly seen in this figure. For electron-proton-$He^{++}$ plasmas, the wave stop gap width increases as $He^{++}$ density increases. Thus waves in a 2% $He^{++}$ plasma might be able to tunnel through the stop gap whereas waves could be localized near the magnetic

equator for a 15% $He^{++}$ plasma because the stop gap is impenetrable. In contrast, the waves do not reach the cut off or resonance locations for Na 15% plasmas and the waves can reach the higher magnetic latitude easily. Therefore, the mode-converted waves can tunnel through the wave stop gap similar to left-handed polarized EMIC waves at Earth [*Johnson et al.*, 1989, 1995; *Johnson* and *Cheng*, 1999] or localized between Buchsbaum locations [*Kim et al.,* 2009] depending on wave tunneling effects.

The preliminary ray-tracing calculations of IBW mode were performed using an electron proton plasma without heavy ion effects. However, $He^{++}$ is believed to be one of the primary ion species present at Mercury. Because Bernstein waves are excited near the harmonics of the heavy ion cyclotron frequencies when heavy ions are included [e.g., *Stix*, 1992] and the detected wave frequencies are located in the range between $f_{cHe++}$ and $f_{cP}$, the heavy ion effects should also be included on the ray-tracing calculations for the IBW mode.

Both the 2D full wave and the ray-tracing calculations also assumed a simple dipole magnetic field model with azimuthal symmetry, whereas the observations shows strong asymmetry structure in MLT on their occurrence. In addition, the 2D full wave calculations also assume a perfectly conducting boundary condition at Mercury's surface rather than realistic conductivity at the surface [*Anderson et al.*, 2014]. Because the boundary condition with finite conductivity can damp the field-line resonance at Earth [*Lee and Takahashi*, 2006], the realistic boundary condition might be important in Mercury's magnetosphere.

Additionally, even though the wavelength is much smaller than the scale length, *Boardsen et al.* [2014a] noted that the sharp drop in group velocity which leads to the pile up of magnetic compressional wave energy probably violates the WKB approximation so full wave modeling is required around the peak compression and the turning points. Existing ray tracing models

typically ignore spatially varying bulk flow velocities and in general cannot handle tunneling and mode conversion. Therefore, although the ion Bernstein mode explanation can qualitatively explain the compressional observations, further quantitative analysis is required to provide better comparisons with data.

Finally, it is necessary to extend the statistical study from *Boardsen et al.* [2012] using more recent magnetic field data from MESSENGER. With the evolution of the MESSENGER orbit over time, the spatial coverage of the inner magnetosphere is significantly better than that used in *Boardsen et al.* [2012], which covered only a few months after orbital insertion. The better coverage allows us to compare the statistics directly at the magnetic equator and along a field line, similar to statistical study of EMIC waves at Earth [e.g., *Min et al.*, 2012], as opposed to having to map observations as was done with the more limited coverage in the previous study.

**Acknowledgements**. The work at the Princeton University was supported by NASA grants (NNH09AM53I, NNH09AK63I, and NNH11AQ46I), NSF grant ATM0902730, and DOE contract DE-AC02-09CH11466. This work at University of Maryland was supported by NASA Planetary Data Analysis Program grant NNX10AU26G and Geoscience grant NNX08AJ78G.

## References

Anderson, B. J., M. H. Acuna, A. Korth, C. L. Purucker, C. L. Johnson, J. A. Slavin, Solomon S. C. and R. L. McNutt (2008), The structure of Mercury's magnetic field from MESSENGER's first flyby, *Science 321*, 82-85.

Anderson, B. J., C. L. Johnson, H. Korth, M. E. Purucker, Winslow R. M., J. A. Slavin, Solomon S. C., R. L. McNutt Jr., J. M. Raines and T. H. Zurbuchen (2011), The Global Magnetic Field of Mercury from MESSENGER Orbital Observations, *Science 333*, 1859-1862, doi: 10.1126/science.1211001.

Anderson, B. J., C. L. Johnson, H. Korth, J. A. Slavin, Winslow R. M., R. J. Phillips, R. L. McNutt Jr. and Solomon S. C. (2014), Steady-state field-aligned currents at Mercury, *Geophys. Res. Lett., 41*, 7444–7452, doi:10.1002/2014GL061677.

Blomberg, L. G. (1997), Mercury's magnetosphere, exosphere and surface : low-frequency field and wave measurements as a diagnostic tool, *Planet. Space Sci. 45*, 143-148.

Boardsen, S. A., B. J. Anderson, M. H. Acuna, J. A. Slavin, H. Korth and Solomon S. C. (2009a), Narrow-band ultra-low-frequency wave observations by MESSENGER during its January 2008 flyby through Mercury's magnetosphere, *Geophys. Res. Lett. 36*, L01104.

Boardsen, S., J. A. Slavin, B. J. Anderson, A. Korth and Solomon S. C. (2009b), Comparison of ultra-low-frequency waves at Mercury under northward and southward IMF, *Geophy. Res. Lett. 36*, L18106.

Boardsen, S. A., S. A. Slavin, B. J. Anderson, H. Korth, D. Schriver and Solomon S. C. (2012), Survey of coherent ~1 Hz waves in Mercury's inner magnetosphere from MESSENGER observations, *J. Geophys. Res. 117*, A00M05, doi:10.1029/2012JA017822.

494 Boardsen, S., E.-H. Kim, J. M. Raines, J. A. Slavin, D. J. Gershman, B. J. Anderson, H. Korth, T. Sundberg, D. Schriver, P. Travnicek and S. C. Solomon (2014a), Ray-tracing of the Ion
496 Bernstein mode in moderately high proton beta ~ 0.1 in Mercury's inner magnetosphere, *submitted to J. Geophysics. Res.*

498 Boardsen, S. A., G. B. Hospodarsky, C. A. Kletzing, R. F. Pfaff, W. S. Kurth, J. R. Wygant and E. A. MacDonald (2014b), Van Allen Probe observations of periodic rising frequencies of
500 the fast magnetosonic mode, *Geophys. Res. Lett.*, doi:10.1002/2014GL062020.

Buchsbaum, S. J. (1960), Ion Resonance in a Multicomponent Plasma, *Phys. Rev. Lett 5*, 495-
502 497.

Chen, L. and A. Hasegawa (1974), Plasma heating by spatial resonance of Alfvén wave, *Phys.*
504 *Fluids 17*, 1399-1403.

Denton, R. E., M. J. Engebretson, A. Keiling, A. P. Walsh, S. P. Gary, P. M. E. Décréau, C. A.
506 Cattell and H. Rème (2010), Multiple harmonic ULF waves in the plasma sheet boundary layer: Instability analysis, *J. Geophys. Res. 115*, A12224, doi:10.1029/2010JA015928.

508 DiBraccio, G. A., J. A. Slavin, S. A. Boardsen, B. J. Anderson, H. Korth, T. H. Zurbuchen, J. M. Raines, D. N. Baker, R. L. McNutt Jr. and S. C. Solomon (2013), MESSENGER
510 observations of magnetopause structure and dynamics at Mercury, *J. Geophys. Res. 118*, doi:10.1002/jgra.50123.

512 Gary, S. P., K. Liu, D. Winske and R. E. Denton (2010), Ion Bernstein instability in the terrestrial magnetosphere: Linear dispersion theory, *J. Geophys. Res. 115*, A12209,
514 doi:10.1029/2010JA015965.

Glassmeier, K.-H., P. N. Mager and D. Y. Klimushkin (2003), Concerning ULF pulsations in
516 Mercury's magnetosphere, *Geophys. Res. Lett. 30*, 1928.

Glassmeier, K.-H., D. Klimushkin, C. Othmer and P. Mager (2004), ULF waves at Mercury:
518 Earth, the giants, and their little brother compared, *Adv. Space Res. 33*, 1875-1883, doi:10.1016/j.asr.2003.04.047.

520 Hasegawa, A., K. H. Tsui and A. S. Assis (1983), A theory of long period magnetic pulsation III—Local field line oscillations, *Geophys. Res. Lett. 10*, 765.

522 Horne, R. B. and R. M. Thorne (1997), Wave heating of $He^+$ by electromagnetic ion cyclotron waves in the magnetosphere: Heating near the $H^+$ - $He^+$ bi-ion resonance frequency, *J.*
524 *Geophys. Res. 102*, 11457.

Johnson, J. R., T. Chang, G. B. Crew and M. Andre (1989), Equatorially generated ULF waves
526 as a source for the turbulence associated with ion conics, *Geophys. Res. Lett. 16*, 1469-1472, doi:10.1029/GL016i012p01469.

528 Johnson, J. R., T. Chang and G. B. Crew (1995), A study of mode conversion in an oxygen-hydrogen plasma, *Phys. Plasmas 2*, 1274-1284.

530 Johnson, J. R. and C. Z. Cheng (1999), Can ion cyclotron waves propagate to the ground?, *Geophys. Res. Lett. 26*, 671-674.

532 Karney, C. F. F., F. W. Perkins and Sun Y. C. (1979), Alfvén resonance Effects on Magnetosonic Modes in Large Tokamaks, *Phys. Rev. Lett. 24*, 1621.

534 Kazakov, Y. O. and T. Fülöp (2013), Mode Conversion of Waves in the Ion-Cyclotron Frequency Range in Magnetospheric Plasmas, *Phys. Rev. Lett. 111*, 125002,
536 doi:10.1103/PhysRevLett.111.125002.

Kim, E.-H. and D.-H. Lee (2003), Resonant absorption of ULF waves near the ion cyclotron
538 frequency: A simulation study, *Geophys. Res. Lett. 30*, 2240.

Kim, E.-H., J. R. Johnson and D.-H. Lee (2008), Resonant absorption of ULF waves at
540 Mercury's magnetosphere, *J. Geophys. Res. 113*, A11207.

Kim, E.-H., J. R. Johnson, I. H. Ciarns and D.-H. Lee (2009) Waves in space plasmas, *in RADIO*
542 *FREQUENCY POWER IN PLASMA: Proceedings of the 18th Topical Conference*.

Kim, E.-H., J. R. Johnson and K.-D. Lee (2011), ULF wave absorption at Mercury, *Geophys.*
544 *Res. Lett. 38*, L16111, doi:10.1029/2011GL048621.

Kim, E.-H., J. R. Johnson, D.-H. Lee and Y. S. Pyo (2013), Field-line resonance structure in
546 Mercury's multi-ion magnetosphere, *Earth, Planets, and Space 65*, 447.

Kim, E.-H., J. R. Johnson, E. Valeo and C. K. Phillips (2015), Global modeling of ULF waves at
548 Mercury, *submitted to Geophys. Res. Lett.*

Klimushkin, D. Y., P. N. Mager and K.-H. Glassmeier (2006), Axisymmetric Alfven resonances
550 in a multi-component plasma at finite ion gyrofrequency, *Ann. Geophys. 24*, 1077-1084.

Lee, D.-H. and R. L. Lysak (1989), Magnetospheric ULF wave coupling in the dipole model -
552 The impulsive excitation, *J. Geophys. Res. 94*, 17097-17103.

Lee, D.-H. and K. Takahashi (2006) MHD Eigenmodes in the Inner Magnetosphere, *in*
554 *Magnetospheric ULF Waves: Synthesis and New Directions*. American Geophysical Union,
Washington, D. C.

556 Lee, D.-H., J. R. Johnson, K. Kim and K.-S. Kim (2008), Effects of heavy ions on ULF wave
resonances near the equatorial region, *J. Geophys. Res. 113*, A11212, doi:10.1029/2008JA
558 013088.

Min, K., J. Lee, K. Keika and W. Li (2012), Global distribution of EMIC waves derived from
560 THEMIS observations, *J. Geophys. Res. 117*, A05219, doi:10.1029/2012JA017515.

Ness, N. F., K. W. Behannon, R. P. Lepping, Y. C. Whang and K. H. Schatten (1974), Magnetic
562 field observations near Mercury: Preliminary results from Mariner 10, *Science 185*, 151-160.

Othmer, C., K.-H. Glassmeier and R. Cramm (1999), Concerning field line resonances in
564 Mercury's magnetosphere, *J. Geophys. Res. 104*, 10369-10378.

Raines, J. M., D. J. Gershman, T. H. Zurbuchen, M. Sarantos, J. A. Slavin, J. A. Gilbert, H.
566 Korth, B. J. Anderson, G. Gloeckler, S. M. Krimigis, D. N. Baker, R. L. McNutt and S. C. Solomon (2013), Distribution and compositional variations of plasma ions in Mercury's
568 space environment: The first three Mercury years of MESSENGER observations, *J. Geophys. Res. 118*, 1604-1619, doi:10.1029/2012JA018073.

570 Raines, J. M., D. J. Gershman, J. A. Slavin, T. H. Zurbuchen, H. Korth, B. J. Anderson and Solo (2014), Structure and dynamics of Mercury'smagnetospheric cusp: MESSENGER
572 measurements of protons and planetary ions, *J. Geophys. Res 119*, 6587–6602, doi:10.1002/2014JA0201.

574 Rönnmark, K., 1982. *WHAMPS: Waves in homogeneous, anisotropic multicomponent plasmas*. Kiruna Geophys. Inst., Kiruna, Sweden.

576 Rönnmark, K. (1984), Ray tracing in dissipative media, *Ann. Geophys. 2*, 57-60.

Russell, C. T. (1989), ULF waves in the Mercury magnetosphere, *Geophys. Res. Lett. 16*, 1253-
578 1256.

Slavin, J. A., M. H. Acu, B. J. Anderson, D. N. Baker, M. Benna, G. Gloeckler, R. E. Gold, G. C.
580 Ho, R. M. Killen, H. Korth, S. M. Krimigis, R. L. McNutt, L. R. Nittler, J. M. Raines, D.

Schriver, S. C. Solomon, R. D. Starr, P. Tr and T. H. Zurbuchen (2008), Mercury's
582 Magnetosphere After MESSENGER's First Flyby, *Science 321*, 85-.

Slavin, J. A., M. H. Acuna, B. J. Anderson, D. N. Baker, M. Benna, S. A. Boardsen, G.
584 Gloeckler, R. E. Gold, G. C. Ho, H. Korth, S. M. Krimigis, R. L. McNutt, J. M. Raines, M. Sarantos, D. Schriver, S. C. Solomon, P. Travnicek and T. H. Zurbuchen (2009),
586 MESSENGER observations of magnetic reconnection in Mercury's magnetosphere, *Science 324*, 606-610, doi:10.1126/science.1172011.

588 Southwood, D. J. (1974), Some features of field line resonances in the magnetosphere, *#planss# 22*, 483-491.

590 Southwood, D. J. (1997), The magnetic field of Mercury, *Plane 45*, 113-117.

Stix, T. H. (1992) *Waves in plasmas*. New York,: American Institute of Physics.

592 Tamao, T. (1965), Transmission and coupling resonance of hydromagnetic disturbances in the nonuniform earth'smagnetosphere, *Sci. Rept Tohoku Univ. 5*, 43.

594 Uberoi, C. (1972), Alfven waves in inhomogeneous magnetic fields, *Phys 15*, 1673.

Winglee, R. M. (1982), Finite frequency effects on magnetosonic wave mode conversion,
596 *Plasma Phys. 24*, 1161.

Wukitch, S. J., Y. Lin, A. Parisot, J. C. Wright, P. T. Bonoli, M. Porkolab, N. Basse, E. Edlund,
598 A. Hubbard, L. Lin, A. Lynn, E. Marmar, D. Mossenssian, P. Phillips and G. Sshilling (2005), Ion cyclotron range of frequency mode conversion physics in Alcator C-Mod:
600 Experimental measurements and modeling, *Phys. Plasmas 12*, 056104.

Zurbuchen, T. H., J. M. Raines, G. Gloeckler, S. M. Krimigis, J. A. Slavin, P. L. Koehn, R. M.
602 Killen, A. L. Sprague, R. L. McNutt Jr. and Solomon S. C. (2008), MESSENGER

observations of the composition of Mercury's ionized exosphere and plasma environment, *Science 321*, 90-92.

Zurbuchen, T. H., J. M. Raines, J. A. Slavin, D. J. Gershman, J. A. Gilbert, G. Gloeckler, B. J. Anderson, D. N. Baker, H. Korth, Krimigis S. M., Sarantos M. S., Schiriver D., R. L. McNutt Jr. and Solomon S. C. (2011), MESSENGER observations of the spatial distribution of planetary ions near Mercury, *Science 333*, 1862-1865, doi: 10.1126/science.1211302.

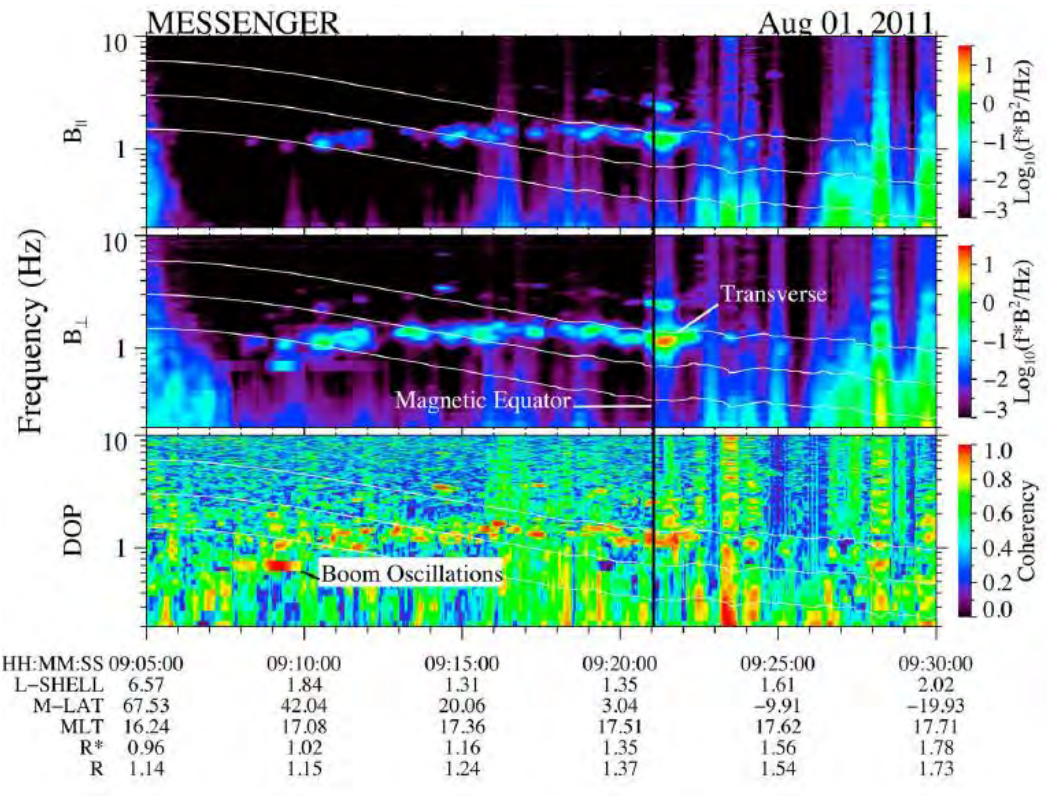


Figure 1. An example of a ULF wave for which the transverse component was dominant at all latitudes, even during equatorial passage. Dynamic spectra of the (top) parallel (compressional) and (middle) perpendicular (transverse) components and (bottom) degree of polarization (DOP) of the magnetic field are shown on August 1 2011. The vertical black line indicates the model magnetic equator. The white curves show the (top to bottom) $H^+$, $He^{++}$, and $He^+$ cyclotron frequencies. The time-axis label L-SHELL is the magnetic L-shell, M-LAT is magnetic latitude in degrees, MLT is magnetic local time in hours, R is the radial position of the spacecraft from planet center in $R_M$, and R* is the radial distance from the offset dipole. Narrow-band harmonic waves are observed in all panels. (Adapted from *Boardsen et al.* [2012])

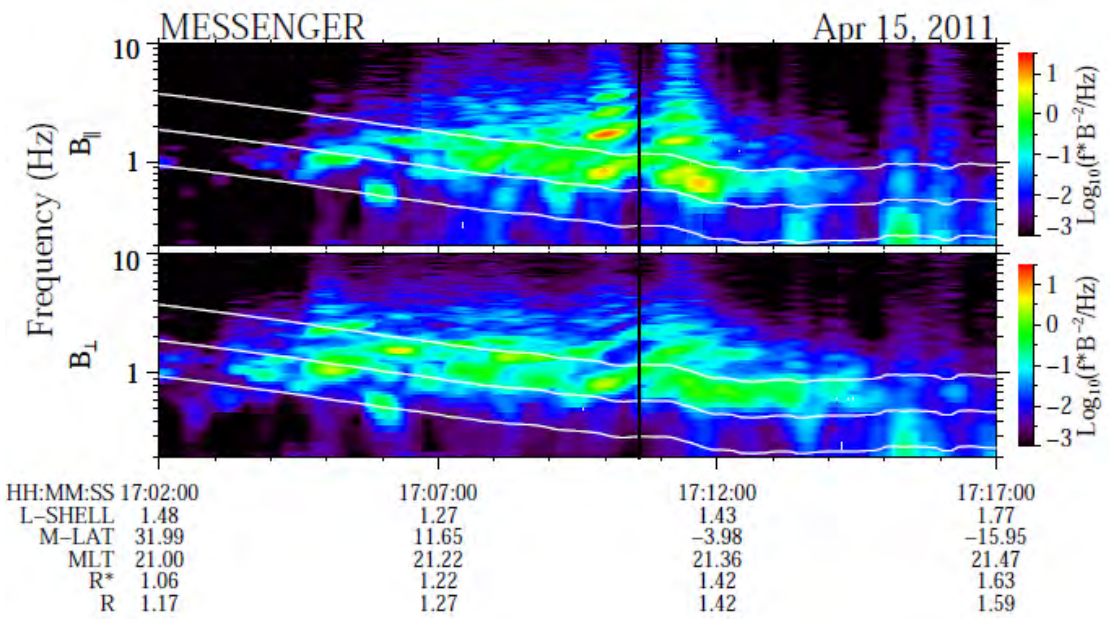


622

624 Figure 2 An example of a ULF wave for which the compressional component was dominant near the crossing of the model magnetic equator. Note that the magnetic compression straddles the

626 model magnetic equator. (Adapted from *Boardsen et al.* [2012])

628

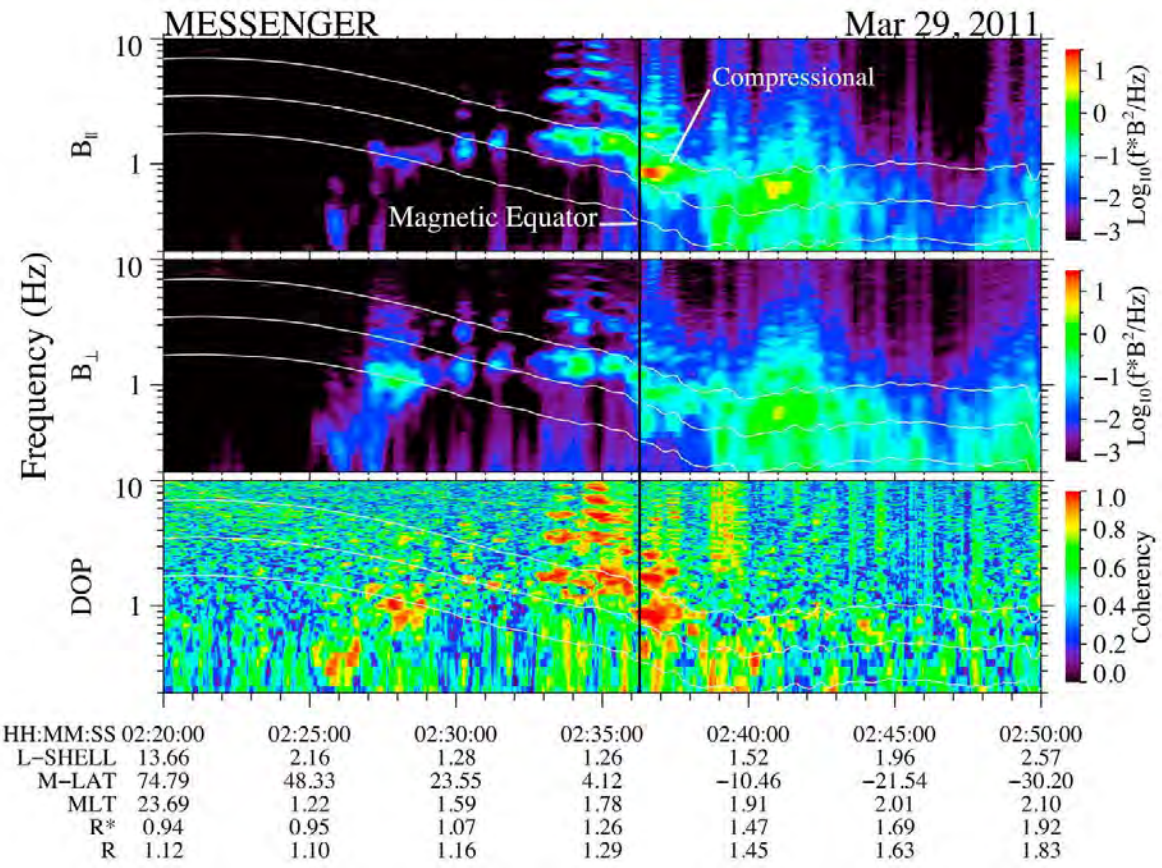


630 Figure 3. An example of ULF waves which are highly compressional near the magnetic equator and transverse away from the magnetic equator. The magnetic compression has a peak around 632 02:36 UT and another peak around 2:42 UT. The magnetic minimum (indicated by the dip in the cyclotron frequencies) is around 02:38 UT suggesting the location of the 634 "true" magnetic equator crossing. (Adapted from *Boardsen et al.* [2012])

636

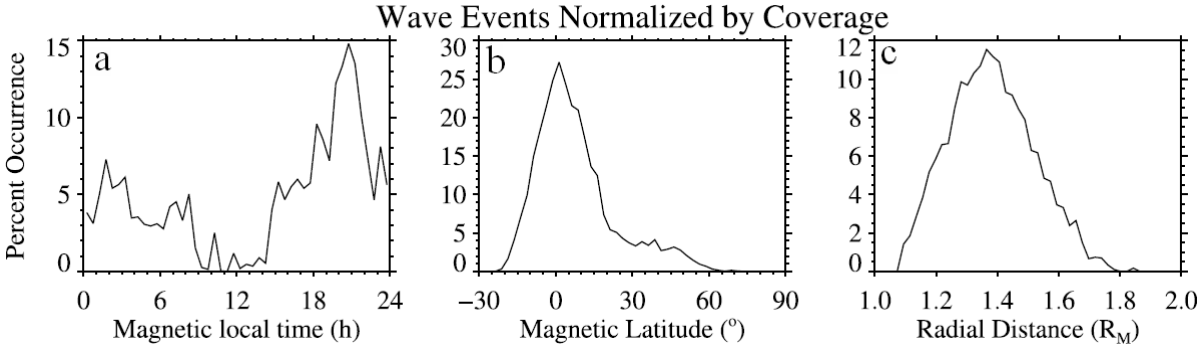


638 Figure 4. Histograms of wave events normalized by coverage as a function of (a) magnetic local time, (b) magnetic latitude, and (c) radial distance (Adapted from *Boardsen et al.* [2012])

640

642

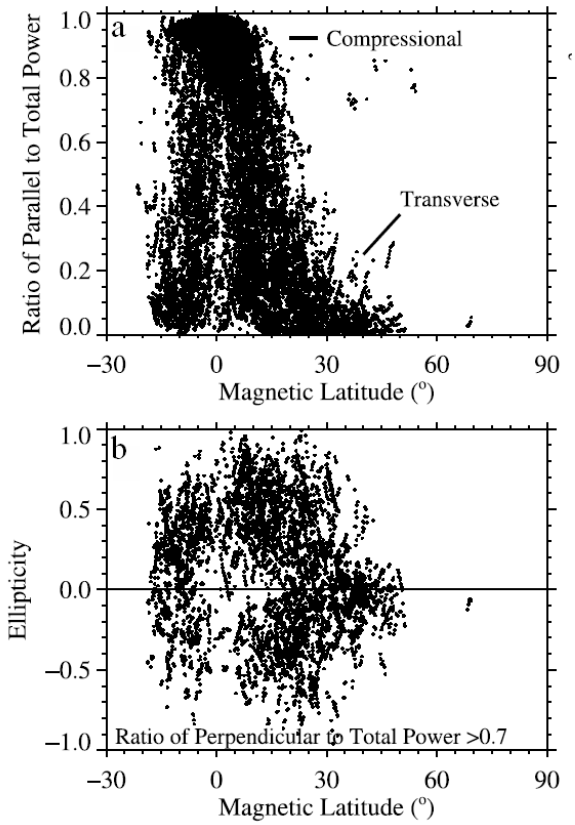


644 Figure 5. (a) Ratio of parallel power to total power versus magnetic latitude for nightside wave events. The waves tend to be compressional near the equator and strongly transverse away from 646 the equator. (b) Wave ellipticity versus magnetic latitude for wave events for which the ratio of transverse power to total power is greater than 0.7 (Adapted from *Boardsen et al.* [2012])

648

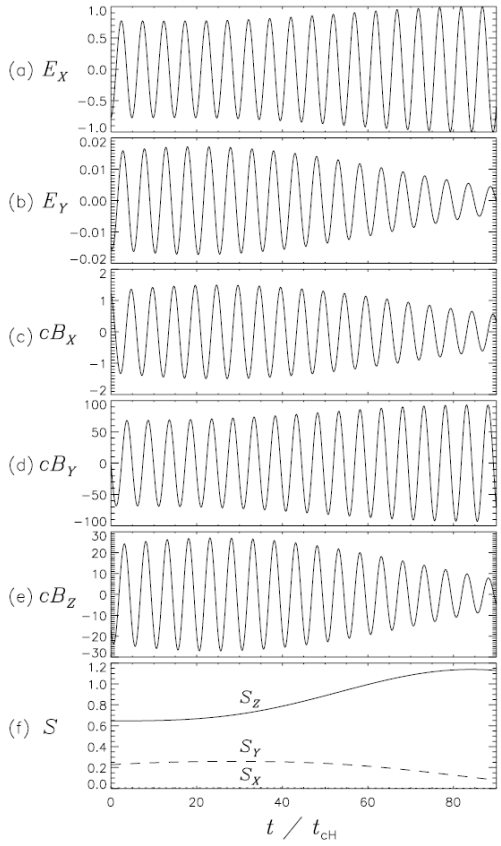


650

Figure 6. (a–e) Time histories of electromagnetic fields and (f) the Poynting flux S of wave at
652 the IIH resonance marked as diamond for $f/f_{cP} = 0.2$. In Figure 6f, the dotted, dashed, and solid lines are $S_x$, $S_y$, and $S_z$, respectively. In this figure, the slab coordinate has been adopted assuming
654 that the plasma inhomogeneity and $\mathbf{B}_0$ lie in $x$ and $z$ direction, respectively. (Adapted from *Kim et al.* [2008])

656

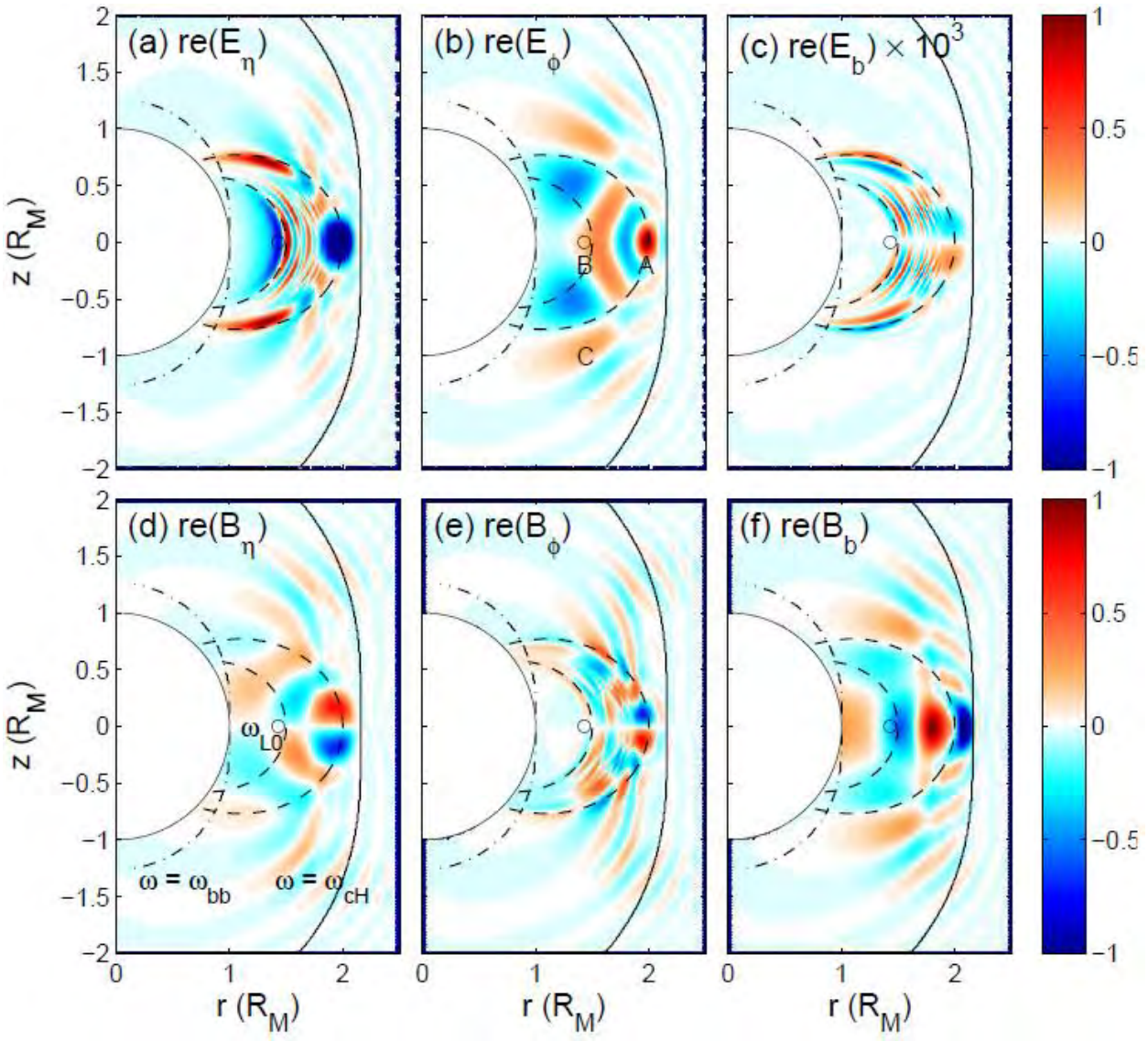


658

Figure 7. Wave solutions if (a-c) electric field and (d-f) magnetic field. Here, $\hat{\mathbf{b}}$ is along the

660 magnetic field line from north to south, $\hat{\boldsymbol{\varphi}}$ is the usual azimuthal direction and $\hat{\boldsymbol{\eta}}$ is normal to the field line pointing outward ($\hat{\boldsymbol{\eta}} = \hat{\mathbf{b}} \times \hat{\boldsymbol{\varphi}}$), with the assumption of $\mathbf{B}_0 \cdot \hat{\boldsymbol{\varphi}} = 0$. The solid lines indicate

662 $\omega=\omega_{ci}$, the dashed-dotted lines indicate $\omega=\omega_{bb}$, and the dashed lines are magnetic field line at $L_M$=1.5 and 2.0, respectively. The circle represents where $\omega=\omega_{L0}$, the FW mode cutoff location

664 at the magnetic equator. (Adapted from *Kim et al.* [2015])

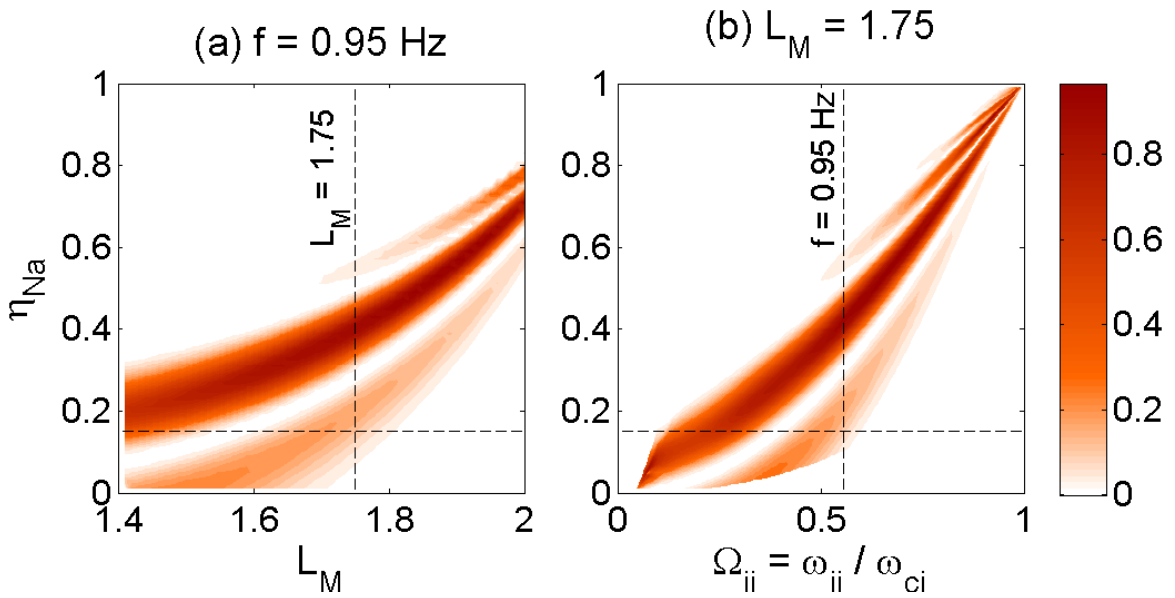


Figure 8. The absorption coefficient as a function of (a) $L_M$ and $\eta_{Na}$ and (b) $\Omega = f / f_{cP}$. The horizontal dashed lines represent where $\eta_{Na} = 15\%$, which is the same condition as 2D full wave calculations [*Kim et al.*, 2015] and the vertical dashed lines are where $L_M = 1.75$ in (a) and $f =$ 0.95 Hz in (b), respectively.

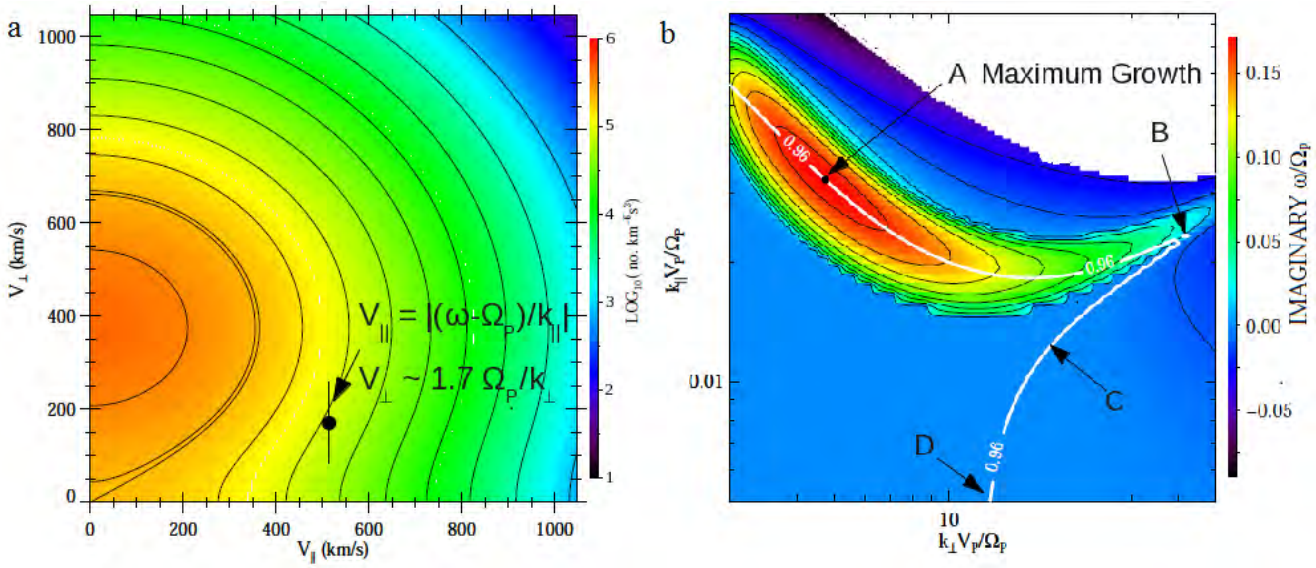


672 Figure 9. (a) A proton distribution function, with a large planetary loss cone, is plotted as a function of $V_\perp$ and $V_\parallel$, which is used to compute the dispersion relation. The region of maximum

674 interaction of protons with these waves at peak growth is indicated. b) The warm plasma solution of the index of refraction curve (white) is plotted versus normalized $k_\parallel$ and $k_\perp$ is overlaid on top

676 of the imaginary dispersion surface (red-green growth, blue damping). This curve contains the peak growth rate (point A). Note that the x-y scales in (b) are different.

678

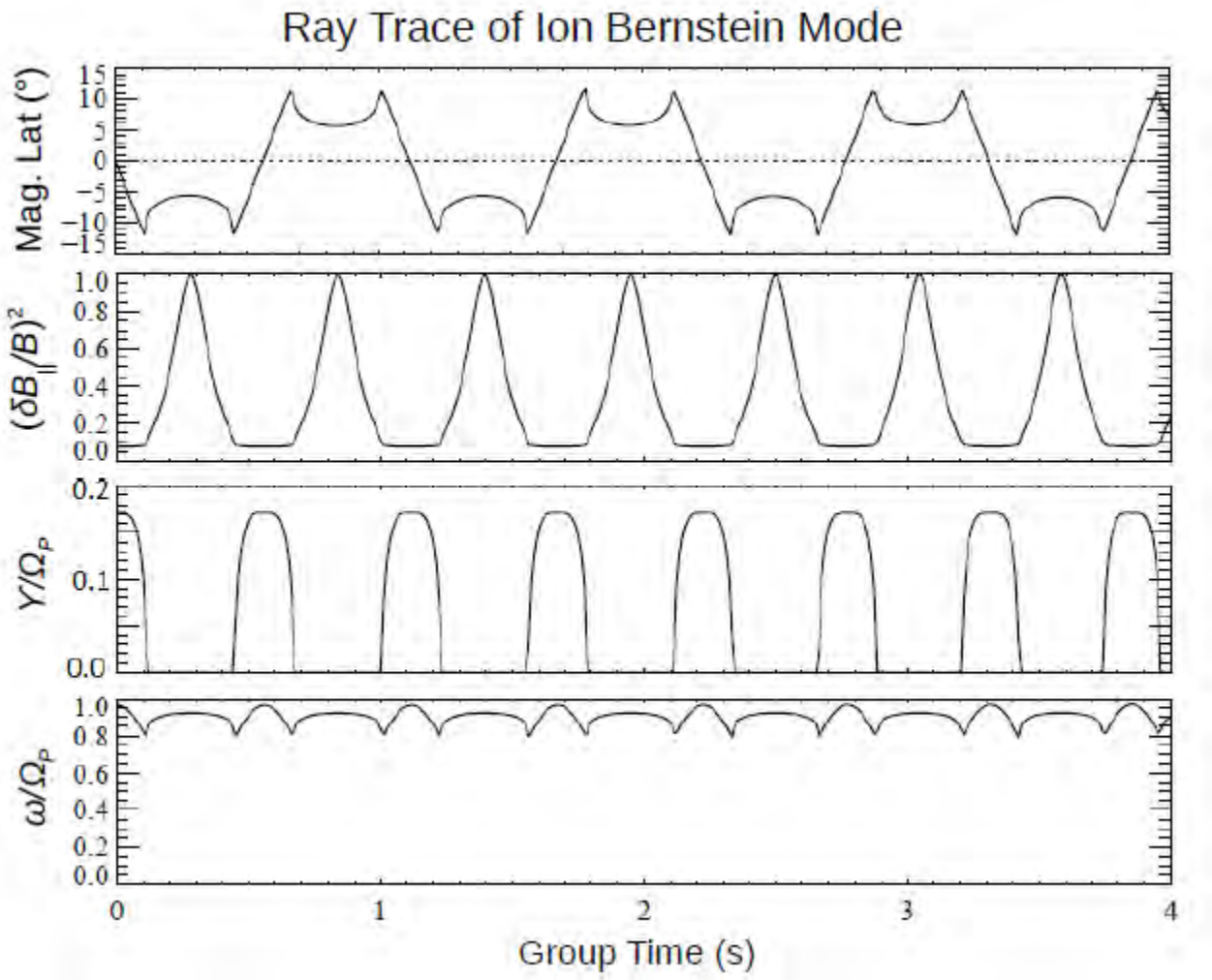


680 Figure 10. Various wave parameters versus group time are plotted. The ray was launched at the magnetic equator, at 1.35 $R_M$, at peak growth rate (wave normal angle of 89.61°). Panel a) is the
682 magnetic latitude, b) is the magnetic compressibility, c) is growth rate ($\gamma$), and d) is the wave frequency ($\omega$) both normalized by the angular proton cyclotron frequency ($\Omega_P$). The magnetic
684 compressibility maximizes off the magnetic equator consistent with observations in Figure Y1. (Adapted from *Boardsen et al.* [2014])

686

688

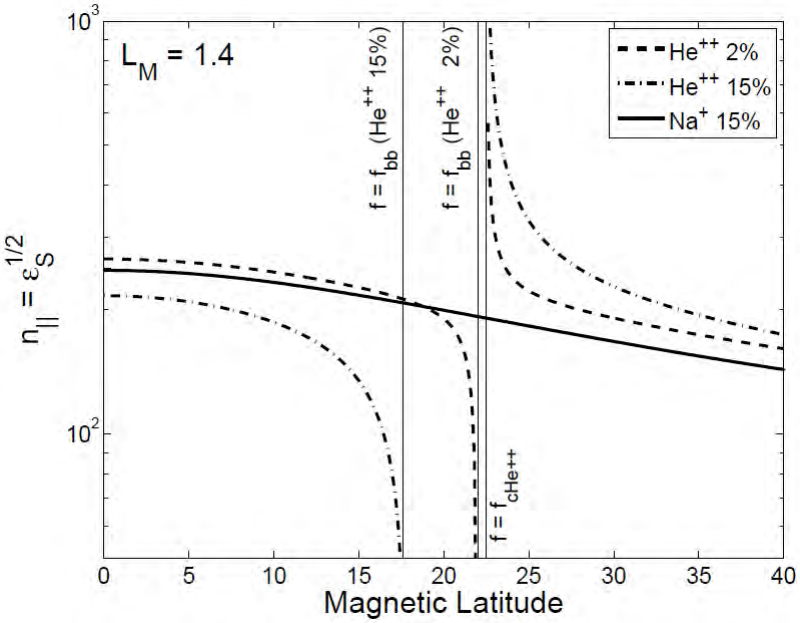


690 Figure 11. The dispersion relation ( $n_{\|}^2 = \varepsilon_S$ ) of the IIH waves along the magnetic field line at $L_M$=1.4 for 2% (dashed) and 15% $He^{++}$ (dotted-dashed) or 15% $Na^+$ (solid lines) plasmas. The 692 stop gap between $f_{bb}$ and $f_{cHe++}$ is clearly seen in this figure.

Princeton Plasma Physics Laboratory
Office of Reports and Publications

Managed by
Princeton University

under contract with the
U.S. Department of Energy
(DE-AC02-09CH11466)

P.O. Box 451, Princeton, NJ 08543
Phone: 609-243-2245
Fax: 609-243-2751

E-mail: publications@pppl.gov
Website: http://www.pppl.gov